
E2Former: A Linear-time Efficient and Equivariant Transformer for Scalable Molecular Modeling

Yunyang Li^{*1} Lin Huang^{*2} Zhihao Ding³ Chu Wang³ Xinran Wei² Han Yang² Zun Wang² Chang Liu²
 Yu Shi² Peiran Jin² Jia Zhang² Mark B. Gerstein^{4,1} Tao Qin²

Abstract

Equivariant Graph Neural Networks (EGNNs) have demonstrated significant success in modeling microscale systems, including those in chemistry, biology and materials science. However, EGNNs face substantial computational challenges due to the high cost of constructing edge features via spherical tensor products, making them impractical for large-scale systems. To address this limitation, we introduce E2Former, an equivariant and efficient transformer architecture that incorporates the Wigner $6j$ convolution (Wigner $6j$ Conv). By shifting the computational burden from edges to nodes, the Wigner $6j$ Conv reduces the complexity from $O(|\mathcal{E}|)$ to $O(|\mathcal{V}|)$ while preserving both the model’s expressive power and rotational equivariance. We show that this approach achieves a 7x–30x speedup compared to conventional $SO(3)$ convolutions. Furthermore, our empirical results demonstrate that the derived E2Former mitigates the computational challenges of existing approaches without compromising the ability to capture detailed geometric information. This development could suggest a promising direction for scalable and efficient molecular modeling.

1. Introduction

Molecular simulations span a wide range of computational tasks—including molecular property prediction, Molecular Dynamics (MD), and Monte Carlo (MC) methods—and

^{*}Equal contribution ¹Department of Computer Science, Yale University, New Haven, USA ²Microsoft Research AI4Science ³The Hong Kong Polytechnic University, Hong Kong S.A.R., China ⁴Program in Computational Biology and Biomedical Informatics, Yale University, New Haven, USA . Correspondence to: Lin Huang <hul@microsoft.com>, Jia Zhang <jia.zhang@microsoft.com>, Mark Gerstein <mark@gersteinlab.org>.

serve as indispensable tools for probing the microscopic processes that underpin chemical (Hwang et al., 2015; Karsai et al., 2018; Kundu et al., 2021; 2022), biological (Cellmer et al., 2011), and material systems (Yamakov et al., 2002). While quantum mechanical approaches like Density Functional Theory (DFT) deliver highly accurate results (Hohenberg & Kohn, 1964; Kohn & Sham, 1965), they scale unfavorably with system size (Szabo & Ostlund, 2012), limiting their utility for larger systems. In contrast, machine learning (ML) methodologies (Bartók et al., 2010; 2013; Drautz, 2019) have emerged as a promising alternative, offering a favorable balance between accuracy and computational cost. These methods can dramatically reduce simulation times from days to mere hours or even seconds. A particular family of the models which have gained significant traction in this field is the Equivariant Graph Neural Networks (EGNNs) (Fuchs et al., 2020; Thomas et al., 2018).

Recent Progress of EGNNs. By constructing graph representations of atomic environments and embedding symmetry considerations—such as invariance under rotations and reflections—directly into the model architecture, EGNNs achieve a high degree of fidelity. Early architectures like SchNet (Schütt et al., 2018) pioneered rotationally invariant feature embeddings. Subsequent innovations, including geometric message-passing frameworks leveraging bond angles and dihedral angles (Gasteiger et al., 2020; 2021), E(3)-equivariant message passing (Batzner et al., 2022), and SE(3)-Transformers (Fuchs et al., 2020; Liao & Smidt, 2022) have steadily improved both accuracy and scalability. Meanwhile, further optimizations (Batatia et al., 2022; Luo et al., 2024; Passaro & Zitnick, 2023; Liao et al., 2023) continue to bolster accuracy and computational efficiency.

Despite significant advancements, EGNNs incur high computational costs, primarily due to constructing edge features via Clebsch–Gordan tensor products between node irreps and spherical harmonics (Fig. 1(a)). These higher-order features, enabled by irreps with angular momentum $L > 1$, capture complex geometric relationships and rotational symmetries, thereby enhancing EGNNs’ expressiveness and ability to model many-body interactions (Thomas et al., 2018; Smidt et al., 2021). As a result, EGNNs better repre-

sent asymmetries and degeneracies, improving both generalization and data efficiency (Smidt et al., 2021). However, the reliance on spherical-equivariant operations involving expensive tensor products results in computational complexities that scale with both the number of edges $|\mathcal{E}|$ and the angular momentum cutoff L , leading to costs of $O(|\mathcal{E}|L^3)$ or $O(|\mathcal{E}|L^6)$. This scalability bottleneck confines spherical-equivariant methods to smaller molecular systems.

In this work, we introduce the Wigner $6j$ convolution (Wigner $6j$ Conv, Figure 2), a spherical-equivariant method that uses Wigner $6j$ symbols (Lai & Chiu, 1990; Maximon, 2010; Edmonds, 1996) to shift computation from edges to nodes, reducing complexity to $O(|\mathcal{V}|)$ while maintaining expressive power and rotational equivariance. As shown in Figure 1(b), our model demonstrates better scaling behavior than the SO(3) convolution, achieving 7x to 30x speed-up giving the sparsity of the molecular graph. Our contribution can be summarized as follows:

- We introduce the Wigner $6j$ convolution, a spherical-equivariant technique that reduces the computational complexity from $O(|\mathcal{E}|)$ to $O(|\mathcal{V}|)$, enabling the modeling of larger molecular systems without compromising the network’s expressive power or symmetry properties.
- We propose E2Former, an equivariant and efficient Transformer architecture specifically designed for scalable molecular modeling. E2Former leverages the novel Wigner $6j$ convolution to maintain rotational equivariance while significantly enhancing computational efficiency.
- Through extensive experiments on benchmark datasets such as OC20, OC22, and SPICE, E2Former achieves state-of-the-art accuracy in predicting molecular energies and forces. Additionally, E2Former demonstrates better efficiency and scalability compared to existing spherical-equivariant methods. Finally, we evaluated E2Former in molecular dynamics, where it achieves DFT-level accuracy with faster speed, outperforming state-of-the-art empirical potential methods. This suggests its potential in advancing large-scale molecular simulations and related applications.

2. Related Work

Equivariant Graph Neural Networks (EGNNs)¹

Symmetry-aware architectures have become central to

¹The term EGNN refers broadly to models that impose rotational, translational, and/or reflection equivariance on graph data. This includes various architectures, such as equivariant graph attention networks and equivariant transformers, which fall under the broader category of EGNNs.

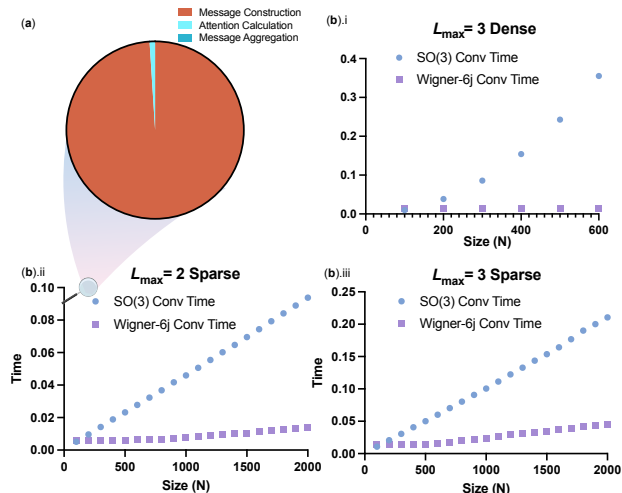


Figure 1. (a) A breakdown of the total computation cost for SO(3) convolution, highlighting that message construction dominates runtime, with a relatively small fraction spent on attention calculation and message aggregation. (b) Time comparisons of SO(3) convolution (blue circles) and Wigner $6j$ convolution (purple squares) as a function of graph size N for different maximum angular momenta (L_{\max}) and sparsity levels. Subplots (b.i) shows dense connectivity at $L_{\max} = 3$ while (b.ii) and (b.iii) show results for sparse connectivity at $L_{\max} = 3$ and $L_{\max} = 2$, respectively. The proposed Wigner $6j$ convolution remains consistently faster than the SO(3) convolution across all tested conditions. Details of the experiments could be found in Sec. 6.1.

machine learning tasks where physical or geometric constraints are crucial. Foundational work on group-equivariant convolutional neural networks (ECNNs) (Cohen & Welling, 2016) established the importance of symmetry constraints, and subsequent theoretical results (Kondor & Trivedi, 2018) demonstrated that convolutional structures and equivariance are inherently linked.

Invariant GNNs. Invariant geometric GNNs have driven state-of-the-art performance in predicting molecular and crystalline properties (Schütt et al., 2018; Sanyal et al., 2018; Chen et al., 2019; Gasteiger et al., 2020; Liu et al., 2022; Gasteiger et al., 2021; Wang et al., 2022) and have been instrumental in advancing protein structure prediction (Jumper et al., 2021).

Cartesian Equivariant GNNs. Building on invariance, Cartesian equivariant GNNs explicitly model transformations in \mathbb{R}^3 , offering greater flexibility. These models have shown strong empirical results in similar domains (Jing et al., 2020; Satorras et al., 2021; Du et al., 2022; Simeon & De Fabritiis, 2024) and have recently evolved to include Cartesian equivariant transformer layers (Frank et al., 2022).

Spherical Equivariant GNNs. Complementing Cartesian approaches, spherical equivariant GNNs leverage spherical

tensors to naturally handle rotational symmetries, relying on the representation theory of $SO(3)$. Recent advancements include $SO(3)$ - and $SE(3)$ -equivariant transformer layers (Fuchs et al., 2020; Liao & Smidt, 2022), efficient interatomic potential calculations (Batzner et al., 2022; Batatia et al., 2022; Musaelian et al., 2023), and optimizations that reduce convolutions in $SO(3)$ to $SO(2)$ (Passaro & Zitnick, 2023). These improvements have enabled strong performance in diverse applications, including geometry, physics, and chemistry (Thomas et al., 2018), dynamic molecular modeling (Anderson et al., 2019), and fluid mechanical modeling (Toshev et al., 2023).

3. Background and Preliminaries

To construct efficient spherical-equivariant message-passing mechanisms, we first establish the mathematical foundations, including spherical harmonics, tensor products of irreducible representations (irreps), and Wigner $6j$ theory, which governs recoupling rules in angular momentum spaces.

Notation. Throughout this paper, we adhere to a consistent system. Greek letters ℓ and m denote angular momentum quantum numbers associated with spherical harmonics $Y_m^{(\ell)}$, where $\ell \geq 0$ and $-\ell \leq m \leq \ell$. All spherical harmonics are considered real-valued functions on \mathbb{R}^3 . Positions of nodes in \mathbb{R}^3 are represented as \vec{r} , while node-level feature matrices are denoted $\mathbf{h}_i \in \mathbb{R}^{s \times d}$, where s represents the spherical dimension and d the feature dimension per spherical component. Irreducible representations (irreps) of $SO(3)$ are indexed by their angular momentum label ℓ . The operation $[\cdot]^{(\ell)}$ is used to extract only the ℓ -th order irreducible component from a representation or tensor product. Clebsch-Gordan Tensor products of irreps are symbolized by \otimes (without any superscripts), and its Wigner $6j$ counterpart is denoted by \otimes^{6j} .

First, we define the spherical harmonics in real space:

Definition 3.1 (Real Spherical Harmonics). Real spherical harmonics are families of homogeneous harmonic polynomials on \mathbb{R}^3 , indexed by two integers $\ell \geq 0$ and $-\ell \leq m \leq \ell$, and expressed in spherical coordinates (r, θ, ϕ) , where:

$$r = \sqrt{x^2 + y^2 + z^2}, \quad \theta = \arccos\left(\frac{z}{r}\right), \quad \phi = \arctan 2(y, x).$$

They are defined by:

$$Y_m^\ell(x, y, z) = \begin{cases} k_m^\ell P_m^\ell(\cos \theta) \cos(m\phi), & m > 0, \\ k_m^\ell P_m^\ell(\cos \theta) \sin(|m|\phi), & m < 0, \\ k_0^\ell P_0^\ell(\cos \theta), & m = 0, \end{cases}$$

where P_m^ℓ are the associated Legendre polynomials, and the constants k_m^ℓ are normalization factors chosen according to the desired convention. For example, in `e3nn` implementation, the real spherical harmonics for $\ell = 2$ take the following form in Cartesian

coordinates:

$$\begin{aligned} Y_{-2}^2(x, y, z) &= xy, & Y_{-1}^2(x, y, z) &= yz, \\ Y_0^2(x, y, z) &= 3z^2 - (x^2 + y^2 + z^2), \\ Y_1^2(x, y, z) &= xz, & Y_2^2(x, y, z) &= x^2 - y^2. \end{aligned}$$

Under a rotation $R \in SO(3)$, these functions transform according to:

$$Y_m^\ell(\vec{r}) \mapsto \sum_{m'=-\ell}^{\ell} D_{m,m'}^{(\ell)}(R) Y_{m'}^\ell(\vec{r}),$$

where $D_{m,m'}^{(\ell)}(R)$ are the Wigner D -matrices. This transformation rule ensures that spherical harmonics of fixed degree ℓ transform properly under the action of $SO(3)$.

Next, we formalize the behavior of irreps under tensor products, which is critical for constructing higher-order spherical harmonics.

Definition 3.2 (Tensor Products of Irreps). Let $U^{(\ell_1)}$ and $U^{(\ell_2)}$ be irreducible representations (irreps) of $SO(3)$. Their tensor product $U^{(\ell_1)} \otimes U^{(\ell_2)}$ decomposes into a direct sum of irreps:

$$U^{(\ell_1)} \otimes U^{(\ell_2)} = \bigoplus_{\ell=|\ell_1-\ell_2|}^{\ell_1+\ell_2} U^{(\ell)}.$$

The decomposition is governed by the **Clebsch-Gordan coefficients**, which specify how each irreducible subrepresentation is extracted. Restricting the tensor product to a specific irreducible component $U^{(\ell_3)}$ is denoted as:

$$\left[U^{(\ell_1)} \otimes U^{(\ell_2)} \right]^{(\ell_3)} = \sum_{\ell_1 m_1, \ell_2 m_2} C_{\ell_1 m_1, \ell_2 m_2}^{\ell_3 m_3} U_{m_1}^{(\ell_1)} U_{m_2}^{(\ell_2)}.$$

To obtain the Clebsch-Gordan coefficients, we introduce the Wigner $3j$ symbol:

Definition 3.3 (Wigner $3j$ Symbols). Wigner $3j$ symbols arise naturally in the coupling of angular momenta in quantum mechanics and the representation theory of the rotation group $SO(3)$. These symbols are denoted as:

$$\begin{pmatrix} \ell_1 & \ell_2 & \ell_3 \\ m_1 & m_2 & m_3 \end{pmatrix},$$

where ℓ_1, ℓ_2, ℓ_3 are nonnegative integers (i.e., $0, 1, 2, \dots$) and m_1, m_2, m_3 are integers satisfying $-\ell_i \leq m_i \leq \ell_i$ for each $i = 1, 2, 3$.

The Wigner $3j$ symbol is defined to be zero unless the following conditions are satisfied:

1. **Angular Momentum Triangle Condition:** $|\ell_1 - \ell_2| \leq \ell_3 \leq \ell_1 + \ell_2$,
2. **Magnetic Quantum Number Sum:** $m_1 + m_2 + m_3 = 0$.

The relationship between the Wigner $3j$ symbols and the Clebsch-Gordan coefficients $C_{\ell_1 m_1, \ell_2 m_2}^{\ell_3 m_3}$ is given by:

$$C_{\ell_1 m_1, \ell_2 m_2}^{\ell_3 m_3} = (-1)^{\ell_1 - \ell_2 + m_3} \sqrt{2\ell_3 + 1} \begin{pmatrix} \ell_1 & \ell_2 & \ell_3 \\ m_1 & m_2 & -m_3 \end{pmatrix}.$$

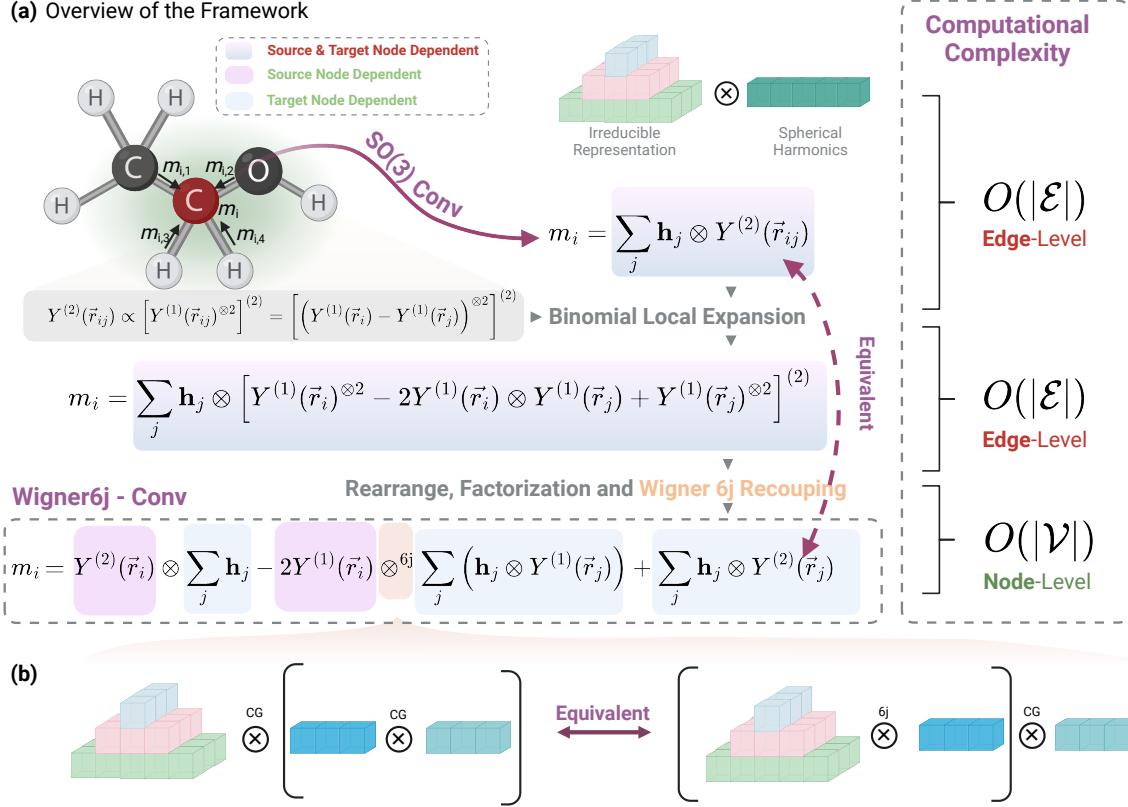


Figure 2. (a) Overview of the Proposed Approach. Rather than performing tensor products over edges by combining node features and distances, E2Former leverages two key concepts: *binomial local expansion* and *Wigner 6j recoupling*. The former represents edge directions in terms of node positions, while the latter reorders the sequence of tensor product operations. Together, the computational complexity of the tensor product is reduced from $O(|\mathcal{E}|)$ to $O(|\mathcal{V}|)$. \otimes denotes the Clebsch-Gordan tensor product, and \otimes^{6j} denotes the CG tensor product where each path is parameterized by a weight governed by the Wigner-6j coefficients. (b) Illustration of two equivalent ways to couple the tensor product of three representations: sequentially coupling two tensors before the third (left) or reordering the coupling sequence (right), with equivalence established via Wigner 6j recoupling.

Commutativity of the Clebsch–Gordan Tensor Product.

The tensor product of two irreducible representations (irreps) $U^{(a)}$ and $U^{(b)}$ of $SO(3)$ is not strictly commutative as a bilinear operation on vector spaces: $U^{(a)} \otimes U^{(b)}$ is not identical to $U^{(b)} \otimes U^{(a)}$. Nonetheless, this operation is *effectively* commutative at the level of irreducible decompositions. Interchanging the order of the factors does not change the set of irreps that appear, although it permutes the corresponding Clebsch–Gordan (CG) coefficients. In particular, we have

$$U^{(a)} \otimes U^{(b)} \cong U^{(b)} \otimes U^{(a)} \cong \bigoplus_{j=|a-b|}^{a+b} U^{(j)}, \quad (1)$$

as well. Thus, while not literally commutative, the tensor product is symmetric with respect to the irreducible content it generates, ensuring that the final decomposition is independent of the order of the factors. This effective commutativity significantly simplifies both theoretical considerations and the design of spherical-equivariant architectures.

Associativity of the Clebsch–Gordan Tensor Product.

For irreps of $SO(3)$, the tensor product operation is associative up to a canonical isomorphism. For any three irreps $U^{(a)}$, $U^{(b)}$, and $U^{(c)}$, we have

$$(U^{(a)} \otimes U^{(b)}) \otimes U^{(c)} \cong U^{(a)} \otimes (U^{(b)} \otimes U^{(c)}),$$

ensuring that the final decomposition into irreps is invariant under regrouping. Although the set of irreps obtained is the same regardless of the association order, the specific CG coefficients that appear depend on the chosen coupling sequence. Wigner 6j symbols facilitate the transition between different coupling orders, enabling the expression of $(U^{(a)} \otimes U^{(b)}) \otimes U^{(c)}$ as $(U^{(a)} \otimes U^{(c)}) \otimes U^{(b)}$, or any other permissible rearrangement, without altering the ultimate irreducible content. Formally, this is expressed as:

$$A \otimes (B \otimes C) = (A \otimes B) \otimes^{6j} C, \quad (2)$$

where \otimes^{6j} denotes a CG tensor product accompanied by a

re-indexing via Wigner $6j$ coefficients.

Definition 3.4 (Wigner $6j$ Symbol). For three irreps $U^{(a)}$, $U^{(b)}$, and $U^{(c)}$ of $\text{SO}(3)$, one can couple them either as $U^{(a)} \otimes (U^{(b)} \otimes U^{(c)})$ or as $(U^{(a)} \otimes U^{(b)}) \otimes U^{(c)}$. The Wigner $6j$ symbol

$$\begin{Bmatrix} a & b & d \\ c & \ell & j \end{Bmatrix}$$

relates these two coupling schemes through the identity

$$\left[U^{(a)} \otimes \left[U^{(b)} \otimes U^{(c)} \right]^{(j)} \right]^{(\ell)} = \sum_d (-1)^{a+b+c+d} \sqrt{(2d+1)(2j+1)} \times \begin{Bmatrix} a & b & d \\ c & \ell & j \end{Bmatrix} \left[U^{(a)} \otimes U^{(b)} \right]^{(d)} \otimes U^{(c)}.$$

To obtain the Wigner $6j$ coefficients:

$$\begin{aligned} \begin{Bmatrix} j_1 & j_2 & j_3 \\ m_1 & m_2 & m_3 \end{Bmatrix} &= \sum_{m_1, m_2, \dots, m_6} (-1)^{\sum_k (j_k - m_k)} \\ &\times \begin{pmatrix} j_1 & j_2 & j_3 \\ -m_1 & -m_2 & -m_3 \end{pmatrix} \begin{pmatrix} j_1 & j_5 & j_6 \\ m_1 & -m_5 & m_6 \end{pmatrix} \\ &\times \begin{pmatrix} j_4 & j_2 & j_6 \\ m_4 & m_2 & -m_6 \end{pmatrix} \begin{pmatrix} j_4 & j_5 & j_3 \\ -m_4 & m_5 & m_3 \end{pmatrix}, \end{aligned}$$

where $\{\cdot\}$ denotes the Wigner $6j$ symbols and (\cdot) represents the Wigner $3j$ symbols.

4. Node-Based Factorization via Wigner $6j$ Recoupling

In this section, we introduce the Attention-Based $\text{SO}(3)$ -Equivariant Node convolution and demonstrate how Wigner $6j$ recoupling facilitates an efficient node-wise computation.

Definition 4.1 (Attention-Based $\text{SO}(3)$ -Equivariant Node convolution). Let $\mathbf{h}_i \in \mathbb{R}^d$ represent the feature vector of node i at layer l , and let $Y^{(\ell)}(\vec{r}_{ij})$ denote the spherical harmonics of the relative direction from node i to node j . The attention-based $\text{SO}(3)$ -equivariant node convolution is defined as follows:

- Edge-Level Attention Coefficients:** For each edge (i, j) , compute attention coefficients α_{ij} based on node features $\mathbf{h}_i, \mathbf{h}_j$, and the geometric embedding $Y^{(\ell)}(\vec{r}_{ij})$. An equivariant scoring function f is used:

$$e_{ij} = f(\mathbf{h}_i, \mathbf{h}_j, Y^{(\ell)}(\vec{r}_{ij})), \quad (3)$$

and the attention coefficients α_{ij} are derived via a softmax:

$$\alpha_{ij} = \frac{\exp(e_{ij})}{\sum_{k \in \mathcal{N}(i)} \exp(e_{ik})}. \quad (4)$$

- Message Passing with $\text{SO}(3)$ -Equivariance:** Aggregate information from neighbors $j \in \mathcal{N}(i)$ by combining features \mathbf{h}_j with directional embeddings $Y^{(\ell)}(\vec{r}_{ij})$:

$$\mathbf{h}_i = \sum_{j \in \mathcal{N}(i)} \alpha_{ij} \left(\mathbf{h}_j \otimes Y^{(\ell)}(\vec{r}_{ij}) \right), \quad (5)$$

Wigner $6j$ convolution. Building upon the attention-based convolution framework, we demonstrate that the convolution operation can be refactored into a node-wise computation using Wigner $6j$ symbols. Specifically, the attention-based $\text{SO}(3)$ convolution can be expressed as:

$$= \sum_{u=0}^{\ell} \underbrace{\left(Y^{(u)}(\vec{r}_i) \right)}_{i\text{-dependent}} \otimes^{6j} \left(\sum_{j \in \mathcal{N}(i)} \alpha_{ij} \underbrace{\left(\mathbf{h}_j \otimes Y^{(\ell-u)}(\vec{r}_{ij}) \right)}_{j\text{-dependent}} \right).$$

Here, the blue boxed terms $Y^{(u)}(\vec{r}_i)$ and \mathbf{h}_j encapsulate all factors dependent on node i . Meanwhile, the red boxed term $Y^{(\ell-u)}(\vec{r}_{ij})$ represents all node- j -dependent factors derived from $(\ell-u)$ harmonics centered at node j . This structured factorization disentangles the node- i -dependent and node- j -dependent components, resulting in a $\mathcal{O}(|V|)$ complexity. Since α_{ij} is a scalar that can be computed efficiently (as shown in Fig. 1(a)), we will omit its further discussion in subsequent sections.

To prove this, we first introduce the concept of *Binomial Local Expansion*, which serves as a key theorem in this factorization.

Theorem 4.2 (Binomial Local Expansion). *Let $\ell = u \geq 1$. Every $\ell = u$ spherical harmonic $Y^{(k)}(\vec{r}_{ij})$ can be expressed as an irreducible subspace of the u -fold tensor product $(Y^{(1)}(\vec{r}_{ij}))^{\otimes u}$. When expanded in terms of node-local terms, this satisfies:*

$$Y_m^{(\ell)}(\vec{r}_{ij}) = \sum_{u=0}^{\ell} (-1)^{\ell-u} \binom{\ell}{u} \left[\left(Y^{(u)}(\vec{r}_i) \right) \otimes \left(Y^{(\ell-u)}(\vec{r}_j) \right) \right]^{(\ell)},$$

Proof Sketch. We first use the following equation

$$Y^{(1)}(\vec{r}_{ij}) = Y^{(1)}(\vec{r}_i) - Y^{(1)}(\vec{r}_j),$$

which expresses the relative direction \vec{r}_{ij} in terms of node-local components. Notice that this equation only holds when $\ell = 1$. Using Definition 3.2, the higher-order spherical harmonics $Y^{\ell=k}$ can be constructed by iteratively coupling $\ell = 1$ representations. Specifically, the $\ell = k$ spherical harmonic is obtained by taking the tensor product of k $\ell = 1$ representations and restricting to the $\ell = k$ irreducible component. This construction is formalized by the following formula:

$$Y^{(k)} = \left[\left(Y^{(1)} \right)^{\otimes k} \right]^{(k)},$$

where the tensor product is taken k times iteratively. Substituting this into $(Y^{(1)}(\vec{r}_{ij}))^{\otimes \ell}$ and expanding via the binomial theorem yields the desired results:

$$\begin{aligned} Y^{(l)}(\vec{r}_{ij}) &= \left[\left(Y^{(1)}(\vec{r}_i) - Y^{(1)}(\vec{r}_j) \right)^{\otimes \ell} \right]^{(l)} \\ &= \left[\sum_{u=0}^{\ell} (-1)^{\ell-u} \binom{\ell}{u} \left(Y^{(u)}(\vec{r}_i) \right) \otimes \left(Y^{(\ell-u)}(\vec{r}_j) \right) \right]^{(l)}. \end{aligned}$$

□

Theorem 4.3 (Node-Based Factorization via Wigner $6j$). *Consider the node features $\mathbf{h}_j \in \mathbb{R}^d$, the attention coefficients α_{ij} , and an ℓ -th order spherical harmonic $Y_m^{(\ell)}(\vec{r}_{ij})$. The $\text{SO}(3)$ convolution with attention is given by:*

$$\sum_{j \in \mathcal{N}(i)} \alpha_{ij} \mathbf{h}_j \otimes Y_m^{(\ell)}(\vec{r}_{ij}).$$

Using Wigner $6j$ recoupling, the ℓ -th order spherical harmonic can be reorganized into a product of an i -dependent irrep (formed from u factors of $Y^{(1)}(\vec{r}_i)$) and a j -dependent part (formed from $(\ell - u)$ factors of $Y^{(1)}(\vec{r}_j)$). Consequently, the factorization becomes:

$$\sum_{j \in \mathcal{N}(i)} \alpha_{ij} \mathbf{h}_j \otimes Y_m^{(\ell)}(\vec{r}_{ij}) = \sum_{u=0}^{\ell} \left(Y^{(u)}(\vec{r}_i) \right) \otimes^{6j} \left(\sum_{j \in \mathcal{N}(i)} \alpha_{ij} \mathbf{h}_j \otimes \left(Y^{(\ell-u)}(\vec{r}_j) \right) \right),$$

where \otimes^{6j} denotes a CG tensor product where the path weight is parameterized by the corresponding Wigner $6j$ coefficients.

Proof Sketch. Binomial Local Expansion. We begin with the expansion of $Y_m^{(\ell)}(\vec{r}_{ij})$ as given in Theorem 4.2:

$$Y_m^{(\ell)}(\vec{r}_{ij}) = \sum_{u=0}^{\ell} (-1)^{\ell-u} \binom{\ell}{u} \left[\left(Y^{(u)}(\vec{r}_i) \right) \otimes \left(Y^{(\ell-u)}(\vec{r}_j) \right) \right]^{(\ell)},$$

where u represents the number of spherical harmonics centered at node i , and $\ell - u$ represents those centered at node j .

Interaction term in $\text{SO}(3)$ convolution. Substituting this expansion into the convolution term:

$$\sum_{j \in \mathcal{N}(i)} \alpha_{ij} \mathbf{h}_j \otimes Y_m^{(\ell)}(\vec{r}_{ij}) = \sum_{j \in \mathcal{N}(i)} \alpha_{ij} \mathbf{h}_j \otimes \left[(-1)^{\ell-u} \binom{\ell}{u} \left(Y^{(u)}(\vec{r}_i) \right) \otimes \left(Y^{(\ell-u)}(\vec{r}_j) \right) \right]^{(\ell)}.$$

Wigner $6j$ recoupling. To reorganize the coupling, we apply Wigner $6j$ symbols, which facilitate the transition from $A \otimes (B \otimes C)$ to $(A \otimes B) \otimes^{6j} C$. Symbolically, letting

$$A = \mathbf{h}_j, \quad B = Y^{(\ell-u)}(\vec{r}_j), \quad C = Y^{(u)}(\vec{r}_i),$$

we start with the original equation. Using the *effective commutativity* (Eq. 1) of the Clebsch-Gordan product: $A \otimes (C \otimes B) = A \otimes (B \otimes C)$,

we then apply the Wigner $6j$ recoupling relation (Eq. 2): $A \otimes (B \otimes C) = (A \otimes B) \otimes^{6j} C$.

Applying this recoupling to the expression above, we achieve the factorized form:

$$\sum_{u=0}^{\ell} \left(Y^{(u)}(\vec{r}_i) \right) \otimes^{6j} \left(\sum_{j \in \mathcal{N}(i)} \alpha_{ij} \mathbf{h}_j \otimes Y^{(\ell-u)}(\vec{r}_j) \right).$$

□

Remark 4.4. The factorized form ensures a clear separation of angular momentum contributions from node i and node j while maintaining full symmetry inherent to $\text{SO}(3)$ -equivariance. Wigner $6j$ recoupling plays a critical role in restructuring the terms, allowing the separation of dependencies on $Y^{(u)}(\vec{r}_i)$ and $Y^{(\ell-u)}(\vec{r}_j)$ without any loss of information or symmetry properties. This separation not only simplifies the mathematical structure but also enhances computational scalability for large-scale graphs, as the precomputed $Y^{(u)}(\vec{r}_i)$ and $Y^{(\ell-u)}(\vec{r}_j)$ reduce the complexity of repeated evaluations during the aggregation process.

5. E2Former Architecture

Model Architecture. Here, we propose *E2Former*, a modular architecture (Appendix Fig. 4(a)) that alternates between E2Attention and feed-forward layers. At its core lies our proposed Wigner $6j$ -based Attention, which employs the Wigner $6j$ convolution as a backend kernel to capture rotational symmetries.

The complete Wigner $6j$ -based attention mechanism is detailed in Algorithm 1. We first precompute spherical harmonics $\mathbf{Y}^{(\ell)}$ up to a maximum order L for the input positions \mathbf{r} . Once the spherical harmonics are obtained, we then iterate over each order k from 0 to L to obtain the attention-modulated outputs. For a given order k , the input features \mathbf{h} are combined with the spherical harmonics $\mathbf{Y}^{(k)}$ through a tensor product operation. The resulting product is then modulated by the attention weights α . Subsequently, the attention-weighted tensor product is *recoupled* via the Wigner $6j$ tensor product, wherein each path is parameterized by Wigner $6j$ coefficients (in contrast to the Clebsch-Gordan tensor product). Finally, summing over all k produces the output irreps, which are used to update node embeddings.

Algorithm 1 Wigner $6j$ -Based Attention

- 1: **Input:** Positions $\mathbf{r} \in \mathbb{R}^{N \times 3}$, input features $\mathbf{h} \in \mathbb{R}^{N \times H \times d \times s}$, attention weights $\alpha \in \mathbb{R}^{N \times N \times H}$ (H for number for heads, s for the number for spherical dimension, d for the number of hidden channels), maximum order L
- 2: **Output:** Output features $\mathbf{h}_{\text{out}} \in \mathbb{R}^{N \times H \times d \times s}$
- 3: **Step 1: Precompute Spherical Harmonics**
- 4: **for** $\ell = 0$ to L **do**
- 5: $\mathbf{Y}^{(\ell)} \leftarrow \text{SH}(\ell, \mathbf{r})$
- 6: **end for**
- 7: **Step 2: Compute Wigner $6j$ tp**
- 8: **for** $k = 0$ to L **do**
- 9: Compute intermediate tensor product:

$$\mathbf{T}_k \leftarrow \text{clebsh.gorden.tp}(\mathbf{h}, \mathbf{Y}^{(k)})$$

- 10: Apply attention weights:

$$\mathbf{T}_k \leftarrow \text{einsum}(\text{"ijh, jhds} \rightarrow \text{ihds"}, \alpha, \mathbf{T}_k)$$

- 11: Recouple terms using Wigner $6j$ symbols:

$$\mathbf{C}_k \leftarrow \text{Wigner6jTP}(\mathbf{T}_k, \mathbf{Y}^{(L-k)})$$

- 12: Update output: $\mathbf{h}_{\text{out}} \leftarrow \mathbf{h}_{\text{out}} + (-1)^k \binom{L}{k} \mathbf{C}_k$
 - 13: **end for**
-

6. Experimental Results

In this section, we first demonstrate the scaling behavior of the proposed Wigner-6j convolution. We then evaluate E2Former, which heavily relies on Wigner-6j convolution, across diverse chemical systems. This evaluation focuses on three standard benchmark datasets: catalysis (OC20, OC22) and molecular conformers (SPICE). Our findings underscore E2Former’s accuracy and computational efficiency.

6.1. Scaling Analysis of Wigner 6j Conv and SO(3) Conv

Here, we recall the results presented in Fig. 1(b), which compares the runtime of Wigner 6j convolution (purple squares) and SO(3) convolution (blue circles). We also ensure that the output of the two networks is *equal* across all test cases given the same input molecular graphs. Specifically, for dense graphs, defined as graphs where every node is connected to all other nodes, at $L_{\max} = 3$ (Fig. 1 (b.i)), the quadratic scaling of SO(3) convolution becomes more pronounced, further widening the performance gap. We compare different graph sizes N , maximum angular momenta L_{\max} , and connectivity patterns. Additionally, for sparse graphs, defined here as graphs with k -nearest neighbor connectivity ($k = 32$), at $L_{\max} = 2$ and $L_{\max} = 3$ (Figs. 1 (b.ii) and (b.iii)), Wigner 6j convolution scales linearly with N , while SO(3) convolution exhibits quadratic scaling, resulting in consistently lower runtimes for Wigner 6j

6.2. Performance on the OC20 Dataset

Dataset Description. The OC20 dataset (Chanussot et al., 2021) comprises 1.2 million DFT relaxations computed using the revised Perdew-Burke-Ernzerhof (RPBE) functional (Hammer et al., 1999). Each system, averaging 73 atoms, represents an adsorbate molecule on a catalyst surface and is designed for the Structure-to-Energy-and-Forces (S2EF) task. This task involves predicting the system’s energy and per-atom forces, with performance evaluated based on the mean absolute error (MAE) of these predictions. We evaluate E2Former by comparing two model variants: the 33M-parameter version and the 67M-parameter version. A summary of the results is presented in Table 1.

E2Former demonstrates strong performance across all model sizes, with 67M variant achieving results comparable to state-of-the-art methods. Notably, the Small variant (33M parameters) maintains competitive accuracy while offering significant computational advantages.

6.3. Performance on the OC22 Dataset

The OC22 dataset (Tran et al., 2023) is specifically designed for studying oxide electrocatalysis. In contrast to OC20, OC22 features DFT total energies, which could serve as a general and versatile DFT surrogate, enabling investigations beyond adsorption energies. We train on the OC22 S2EF-Total task and measure energy and force MAE on the S2EF-Total validation splits. Table 2 summarizes our results on the OC22 S2EF task. E2Former achieves competitive energy and force MAEs and is specifically designed for rapid training and inference. Notably, it converges in just 1,500 GPU hours—only one-third of the runtime required by the SOTA model.

6.4. Performance on the SPICE Dataset

The SPICE dataset (Eastman et al., 2023) comprises small organic molecules and encompasses a diverse array of chemical species with neutral formal charges. The geometries were generated through molecular dynamics simulations using classical force fields, followed by the sampling of various conformations. High-fidelity labeling was achieved at the ω B97M-D3(BJ)/def2-TZVPPD level of calculations. This dataset includes configurations of up to 50 atoms. It was further augmented with larger molecules, ranging from 50 to 90 atoms, derived from the QMugs dataset (Isert et al., 2022), as well as water clusters obtained from simulations of liquid water, thereby enhancing its diversity. Approximately 85% of the SPICE dataset was used for model training, while 15% was allocated for model testing. We evaluate E2Former 33M on the SPICE dataset and a summary of the results is provided in Table 3.

E2Former achieved state-of-the-art performance in most subsets, particularly in datasets with ample data, such as PubChem and DEShaw370-Dimers. Furthermore, compared to the MACE-Large model, E2Former achieves approximately a *fivefold* increase in training speed, thereby further validating its efficiency.

7. Molecular Dynamics Simulation

In this section, we demonstrate the practical utility of E2Former in molecular dynamics simulations. While machine learning methods are extensively used to predict molecular and material properties, accurately simulating the behavior of systems over extended time periods remains a significant challenge. This task requires not only precise predictions at each time step but also long-term stability and performance comparable to established methods such as DFT and empirical potential models.

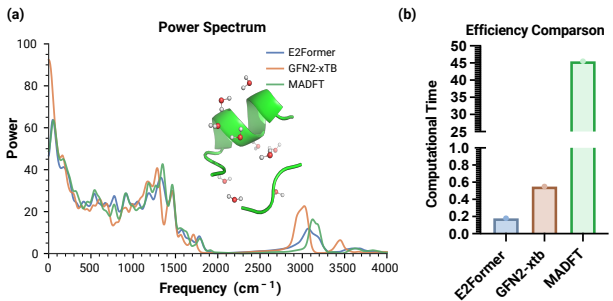


Figure 3. (a) Power spectra comparison across computational methods: E2Former (blue), GFN2-xTB (orange), and MADFT (green). The graph corresponds to a simulation at NVT ensemble, temperature $T = 300$ K, with a time step of 1 fs. A structural overlay of the simulated system is displayed for context. (b) Efficiency comparison showing computational time for E2Former, GFN2-xtb, and MADFT. E2Former demonstrates the lowest computational time. The y-axis denotes the computation time for a single frame.

We began by pretraining E2Former on a large in-house dataset derived from DeShaw (2M) (Donchev et al., 2021) and GEMS (Unke et al., 2024) (2.7M), constituting a *foundational model* on machine-learning force field. To evaluate the model, we performed an NVT ($T = 300$ K) simulation of an amino acid wrapped by water molecules (The structure is shown in Fig. 3(a)), totaling 253 atoms. This evaluation was conducted on a system equipped with

Table 1. Performance on the OC20-2M dataset. Results are reported in Energy (meV) and Force (meV/Å) mean absolute error (MAE). E2Former achieves competitive accuracy and computational efficiency. Approximate training GPU hours are measured on 32G NVIDIA V100 GPUs. The best results are bolded and the second best are highlighted with underline.

Model	# Params (M)	Training GPU Hours	Inference Speed (samples/sec)	Validation	
				Energy MAE (meV)	Force MAE (meV/Å)
GemNet-dT	31	900	50	358	29.50
GemNet-OC	38	1500	38	286	25.70
SCN	126	3000	5	279	21.90
eSCN	51	2200	19	283	<u>20.50</u>
EquiformerV2	85	1800	19	285	20.46
E2Former 33M	<u>33</u>	800	62	<u>275</u>	21.90
E2Former 67M	67	1500	34	270	<u>20.50</u>

Table 2. Performance on the OC22 S2EF task. Results are reported for Energy MAE (meV) and Force MAE (meV/Å) under In Distribution (ID) and Out-Of-Distribution (OOD) splits. Approximate training GPU hours are measured on 32G NVIDIA V100 GPUs. The best results are bolded and the second best are highlighted with underline.

Model	# Params (M)	Training GPU Hours	Energy MAE (meV)		Force MAE (meV/Å)	
			ID	OOD	ID	OOD
GemNet-OC	39	-	545	1011	30.00	40.00
EquiformerV2	122	4500	433	629	22.88	30.70
E2Former 67M	67	1500	<u>491</u>	<u>724</u>	<u>25.98</u>	<u>36.45</u>

Table 3. Performance comparison on the SPICE dataset with actual training time and dataset sizes. Results are reported in Energy (E, meV/atom) and Force (F, meV/Å) MAE. Approximate training GPU hours are measured on 80G NVIDIA A100 GPUs.

Dataset Name (Size)	Training Time (gpu hours)	PubChem (33884)		Monomers (889)		Dimers (13896)		Dipeptides (1025)		SolvatedAminoAcids (52)		Water (84)		Qmugs (144)		All	
		E	F	E	F	E	F	E	F	E	F	E	F	E	F	E	F
MACE Small	168	1.41	35.68	1.04	17.63	0.98	16.31	0.84	25.07	1.60	38.56	1.67	28.53	1.03	41.45	1.27	29.76
MACE Medium	240	0.91	20.57	0.63	9.36	0.58	9.02	0.52	14.27	1.21	23.26	0.76	15.27	0.69	23.58	0.80	17.03
MACE Large	336	0.88	14.75	0.59	6.58	0.54	6.62	0.42	10.19	0.98	19.43	0.83	13.57	0.45	16.93	0.77	12.26
E2Former 33M	70	0.67	8.9	0.49	7.1	0.43	4.01	0.51	5.63	1.1	19.2	0.96	13.52	0.65	10.2	0.60	7.46

a single NVIDIA A100 GPU and an AMD EPYC 7V13 24-core CPU. Over the course of 10,000 simulation time steps (1fs per step), we compared the trajectory’s power spectrum obtained from E2Former, CUDA-accelerated DFT (Ju et al., 2024)- namely, the MADFT software and state-of-the-art empirical potential methods. Fig. 3(a) illustrates the results.

The evaluation demonstrates that E2Former exhibits long-term stability in molecular simulations. The power spectrum shows that E2Former predictions align closely with those of the DFT baseline. In contrast, empirical methods such as GFN2-xTB (Banwarth et al., 2019) show significant deviations in high-frequency regions, particularly near 3,000 and 3,500 frequencies. These high-frequency components are critical as they provide insights into bond vibrations (Ditler & Lubner, 2022) and molecular stability (Chng et al., 2024), underscoring the ability of E2Former to effectively extrapolate across the molecular potential energy surface.

To assess computational efficiency, we compare runtime across methods, which is depicted in Fig. 3(b). E2Former achieves a computational speed approximately 1,000 times faster than DFT, and around 2 times faster than GFN2-xTB.

Collectively, these findings highlight E2Former’s efficiency and accuracy, making it ideal for large-scale molecular simulations. Its capacity to learn molecular potential energy surfaces could potentially address key challenges in molecular dynamics.

8. Conclusion and Future Work

We introduced E2Former, an efficient and scalable Transformer architecture for molecular modeling. By leveraging the Wigner $\hat{6}_j$ convolution, E2Former shifts computation from edges to nodes, reducing complexity from $O(|\mathcal{E}|)$ to $O(|\mathcal{V}|)$ while maintaining rotational equivariance and expressive power. E2Former demonstrated state-of-the-art performance across OC20, OC22, and SPICE benchmarks, achieving high accuracy in energy and force prediction with significantly improved computational efficiency. Its ability to scale effectively to large molecular systems positions it as a robust tool for advancing computational biology, drug discovery, and materials science.

Future work could focus on optimizing E2Former for emerging hardware accelerators and integrating kernelized Euclidean attention (Frank et al., 2024) to further enhance its performance. Combining Wigner- $\hat{6}_j$ Conv with $SO(2)$ convolution could further bolster the model’s efficiency. Scaling to the real-world all-atom protein systems will also be investigated. In conclusion, E2Former aims to balance accuracy and efficiency, providing a potentially scalable and precise approach for molecular simulations.

Impact Statement

This paper presents work whose goal is to advance the field of Machine Learning for scientific discovery. There are many potential societal consequences of our work, none of which we feel must be specifically highlighted here.

References

- Anderson, B., Hy, T. S., and Kondor, R. Cormorant: Covariant molecular neural networks. *Advances in neural information processing systems*, 32, 2019.
- Bannwarth, C., Ehlert, S., and Grimme, S. Gfn2-xtb—an accurate and broadly parametrized self-consistent tight-binding quantum chemical method with multipole electrostatics and density-dependent dispersion contributions. *Journal of chemical theory and computation*, 15(3):1652–1671, 2019.
- Bartók, A. P., Payne, M. C., Kondor, R., and Csányi, G. Gaussian approximation potentials: The accuracy of quantum mechanics, without the electrons. *Physical review letters*, 104(13):136403, 2010.
- Bartók, A. P., Kondor, R., and Csányi, G. On representing chemical environments. *Physical Review B—Condensed Matter and Materials Physics*, 87(18):184115, 2013.
- Batatia, I., Kovacs, D. P., Simm, G. N. C., Ortner, C., and Csanyi, G. MACE: Higher order equivariant message passing neural networks for fast and accurate force fields. In Oh, A. H., Agarwal, A., Belgrave, D., and Cho, K. (eds.), *Advances in Neural Information Processing Systems*, 2022. URL <https://openreview.net/forum?id=YPpSngE-ZU>.
- Batzner, S., Musaelian, A., Sun, L., Geiger, M., Mailoa, J. P., Kornbluth, M., Molinari, N., Smidt, T. E., and Kozinsky, B. E(3)-equivariant graph neural networks for data-efficient and accurate interatomic potentials. *Nature communications*, 13(1):2453, 2022.
- Cellmer, T., Buscaglia, M., Henry, E. R., Hofrichter, J., and Eaton, W. A. Making connections between ultrafast protein folding kinetics and molecular dynamics simulations. *Proceedings of the National Academy of Sciences*, 108(15):6103–6108, 2011.
- Chanussot, L., Das, A., Goyal, S., Lavril, T., Shuaibi, M., Riviere, M., Tran, K., Heras-Domingo, J., Ho, C., Hu, W., et al. Open catalyst 2020 (oc20) dataset and community challenges. *Acs Catalysis*, 11(10):6059–6072, 2021.
- Chen, C., Ye, W., Zuo, Y., Zheng, C., and Ong, S. P. Graph networks as a universal machine learning framework for molecules and crystals. *Chemistry of Materials*, 31(9):3564–3572, 2019.
- Chng, C.-P., Dowd, A., Mechler, A., and Hsia, K. J. Molecular dynamics simulations reliably identify vibrational modes in far-ir spectra of phospholipids. *Physical Chemistry Chemical Physics*, 2024.
- Cohen, T. and Welling, M. Group equivariant convolutional networks. In Balcan, M. F. and Weinberger, K. Q. (eds.), *Proceedings of The 33rd International Conference on Machine Learning*, volume 48 of *Proceedings of Machine Learning Research*, pp. 2990–2999, New York, New York, USA, 20–22 Jun 2016. PMLR. URL <https://proceedings.mlr.press/v48/cohen16.html>.
- Ditler, E. and Lubner, S. Vibrational spectroscopy by means of first-principles molecular dynamics simulations. *Wiley Interdisciplinary Reviews: Computational Molecular Science*, 12(5):e1605, 2022.
- Donchev, A. G., Taube, A. G., Decolvenaere, E., Hargus, C., McGibbon, R. T., Law, K.-H., Gregersen, B. A., Li, J.-L., Palmo, K., Siva, K., et al. Quantum chemical benchmark databases of gold-standard dimer interaction energies. *Scientific data*, 8(1):55, 2021.
- Drautz, R. Atomic cluster expansion for accurate and transferable interatomic potentials. *Physical Review B*, 99(1):014104, 2019.
- Du, W., Zhang, H., Du, Y., Meng, Q., Chen, W., Zheng, N., Shao, B., and Liu, T.-Y. Se (3) equivariant graph neural networks with complete local frames. In *International Conference on Machine Learning*, pp. 5583–5608. PMLR, 2022.
- Eastman, P., Behara, P. K., Dotson, D. L., Galvelis, R., Herr, J. E., Horton, J. T., Mao, Y., Chodera, J. D., Pritchard, B. P., Wang, Y., et al. Spice, a dataset of drug-like molecules and peptides for training machine learning potentials. *Scientific Data*, 10(1):11, 2023.
- Edmonds, A. R. *Angular momentum in quantum mechanics*, volume 4. Princeton university press, 1996.
- Frank, J. T., Unke, O. T., and Müller, K.-R. So3krates—self-attention for higher-order geometric interactions on arbitrary length-scales. *arXiv preprint arXiv:2205.14276*, 2022.
- Frank, J. T., Chmiela, S., Müller, K.-R., and Unke, O. T. Euclidean fast attention: Machine learning global atomic representations at linear cost. *arXiv preprint arXiv:2412.08541*, 2024.
- Fuchs, F., Worrall, D., Fischer, V., and Welling, M. Se (3)-transformers: 3d roto-translation equivariant attention networks. *Advances in Neural Information Processing Systems*, 33:1970–1981, 2020.
- Gasteiger, J., Groß, J., and Günnemann, S. Directional message passing for molecular graphs. *arXiv preprint arXiv:2003.03123*, 2020.
- Gasteiger, J., Becker, F., and Günnemann, S. Gemnet: Universal directional graph neural networks for molecules. *Advances in Neural Information Processing Systems*, 34:6790–6802, 2021.
- Hammer, B., Hansen, L. B., and Nørskov, J. K. Improved adsorption energetics within density-functional theory using revised Perdew-Burke-Ernzerhof functionals. *Physical Review B*, 59(11):7413, 1999.
- Hohenberg, P. and Kohn, W. Inhomogeneous electron gas. *Physical review*, 136(3B):B864, 1964.
- Hwang, G. S., Stowe, H. M., Paek, E., and Manogaran, D. Reaction mechanisms of aqueous monoethanolamine with carbon dioxide: a combined quantum chemical and molecular dynamics study. *Physical Chemistry Chemical Physics*, 17(2):831–839, 2015.
- Isert, C., Atz, K., Jiménez-Luna, J., and Schneider, G. Qmugs, quantum mechanical properties of drug-like molecules. *Scientific Data*, 9(1):273, 2022.
- Jing, B., Eismann, S., Suriana, P., Townshend, R. J. L., and Dror, R. Learning from protein structure with geometric vector perceptrons. In *International Conference on Learning Representations*, 2020.

- Ju, F., Wei, X., Huang, L., Jenkins, A. J., Xia, L., Zhang, J., Zhu, J., Yang, H., Shao, B., Dai, P., et al. Acceleration without disruption: Dft software as a service. *Journal of Chemical Theory and Computation*, 20(24):10838–10851, 2024.
- Jumper, J., Evans, R., Pritzel, A., Green, T., Figurnov, M., Ronneberger, O., Tunyasuvunakool, K., Bates, R., Žídek, A., Potapenko, A., et al. Highly accurate protein structure prediction with alphafold. *Nature*, 596(7873):583–589, 2021.
- Karsai, F., Engel, M., Flage-Larsen, E., and Kresse, G. Electron-phonon coupling in semiconductors within the gw approximation. *New Journal of Physics*, 20(12):123008, 2018.
- Kohn, W. and Sham, L. J. Self-consistent equations including exchange and correlation effects. *Physical review*, 140(4A):A1133, 1965.
- Kondor, R. and Trivedi, S. On the generalization of equivariance and convolution in neural networks to the action of compact groups. In Dy, J. and Krause, A. (eds.), *Proceedings of the 35th International Conference on Machine Learning*, volume 80 of *Proceedings of Machine Learning Research*, pp. 2747–2755. PMLR, 10–15 Jul 2018. URL <https://proceedings.mlr.press/v80/kondor18a.html>.
- Kundu, A., Govoni, M., Yang, H., Ceriotti, M., Gygi, F., and Galli, G. Quantum vibronic effects on the electronic properties of solid and molecular carbon. *Physical Review Materials*, 5(7):L070801, 2021.
- Kundu, A., Song, Y., and Galli, G. Influence of nuclear quantum effects on the electronic properties of amorphous carbon. *Proceedings of the National Academy of Sciences*, 119(31):e2203083119, 2022.
- Lai, S.-T. and Chiu, Y.-N. Exact computation of the 3-j and 6-j symbols. *Computer physics communications*, 61(3):350–360, 1990.
- Langley, P. Crafting papers on machine learning. In Langley, P. (ed.), *Proceedings of the 17th International Conference on Machine Learning (ICML 2000)*, pp. 1207–1216, Stanford, CA, 2000. Morgan Kaufmann.
- Liao, Y.-L. and Smidt, T. Equiformer: Equivariant graph attention transformer for 3d atomistic graphs. *arXiv preprint arXiv:2206.11990*, 2022.
- Liao, Y.-L., Wood, B., Das, A., and Smidt, T. Equiformerv2: Improved equivariant transformer for scaling to higher-degree representations. *arxiv preprint arxiv:2306.12059*, 2023.
- Liu, Y., Wang, L., Liu, M., Lin, Y., Zhang, X., Oztekin, B., and Ji, S. Spherical message passing for 3d molecular graphs. In *International Conference on Learning Representations (ICLR)*, 2022.
- Luo, S., Chen, T., and Krishnapriyan, A. S. Enabling efficient equivariant operations in the fourier basis via gaunt tensor products. In *The Twelfth International Conference on Learning Representations*, 2024. URL <https://openreview.net/forum?id=mhyQXJ6JsK>.
- Maximon, L. C. 3j, 6j, 9j symbols., 2010.
- Musaelian, A., Batzner, S., Johansson, A., Sun, L., Owen, C. J., Kornbluth, M., and Kozinsky, B. Learning local equivariant representations for large-scale atomistic dynamics. *Nature Communications*, 14(1):579, 2023.
- Passaro, S. and Zitnick, C. L. Reducing so (3) convolutions to so (2) for efficient equivariant gnns. In *International Conference on Machine Learning*, pp. 27420–27438. PMLR, 2023.
- Sanyal, S., Balachandran, J., Yadati, N., Kumar, A., Rajagopalan, P., Sanyal, S., and Talukdar, P. Mt-cgcnn: Integrating crystal graph convolutional neural network with multitask learning for material property prediction. *arXiv preprint arXiv:1811.05660*, 2018.
- Satorras, V. G., Hoogeboom, E., and Welling, M. E (n) equivariant graph neural networks. In *International conference on machine learning*, pp. 9323–9332. PMLR, 2021.
- Schütt, K. T., Sauceda, H. E., Kindermans, P.-J., Tkatchenko, A., and Müller, K.-R. Schnet—a deep learning architecture for molecules and materials. *The Journal of Chemical Physics*, 148(24):241722, 2018.
- Simeon, G. and De Fabritiis, G. Tensornet: Cartesian tensor representations for efficient learning of molecular potentials. *Advances in Neural Information Processing Systems*, 36, 2024.
- Smidt, T. E., Geiger, M., and Miller, B. K. Finding symmetry breaking order parameters with euclidean neural networks. *Phys. Rev. Res.*, 3:L012002, Jan 2021. doi: 10.1103/PhysRevResearch.3.L012002. URL <https://link.aps.org/doi/10.1103/PhysRevResearch.3.L012002>.
- Szabo, A. and Ostlund, N. S. *Modern quantum chemistry: introduction to advanced electronic structure theory*. Courier Corporation, 2012.
- Thomas, N., Smidt, T., Kearnes, S., Yang, L., Li, L., Kohlhoff, K., and Riley, P. Tensor field networks: Rotation-and translation-equivariant neural networks for 3d point clouds. *arXiv preprint arXiv:1802.08219*, 2018.
- Toshev, A. P., Galletti, G., Brandstetter, J., Adami, S., and Adams, N. A. E (3) equivariant graph neural networks for particle-based fluid mechanics. *arXiv preprint arXiv:2304.00150*, 2023.
- Tran, R., Lan, J., Shuaibi, M., Wood, B. M., Goyal, S., Das, A., Heras-Domingo, J., Kolluru, A., Rizvi, A., Shoghi, N., et al. The open catalyst 2022 (oc22) dataset and challenges for oxide electrocatalysts. *ACS Catalysis*, 13(5):3066–3084, 2023.
- Unke, O. T., Stöhr, M., Ganscha, S., Unterthiner, T., Maennel, H., Kashubin, S., Ahlin, D., Gastegger, M., Medrano Sandonas, L., Berryman, J. T., et al. Biomolecular dynamics with machine-learned quantum-mechanical force fields trained on diverse chemical fragments. *Science Advances*, 10(14):eadn4397, 2024.
- Wang, L., Liu, Y., Lin, Y., Liu, H., and Ji, S. ComENet: Towards complete and efficient message passing for 3d molecular graphs. In Oh, A. H., Agarwal, A., Belgrave, D., and Cho, K. (eds.), *Advances in Neural Information Processing Systems*, 2022. URL <https://openreview.net/forum?id=mCzMQeWSFJ>.
- Yamakov, V., Wolf, D., Phillpot, S. R., Mukherjee, A. K., and Gleiter, H. Dislocation processes in the deformation of nanocrystalline aluminium by molecular-dynamics simulation. *Nature materials*, 1(1):45–49, 2002.

A. Appendix

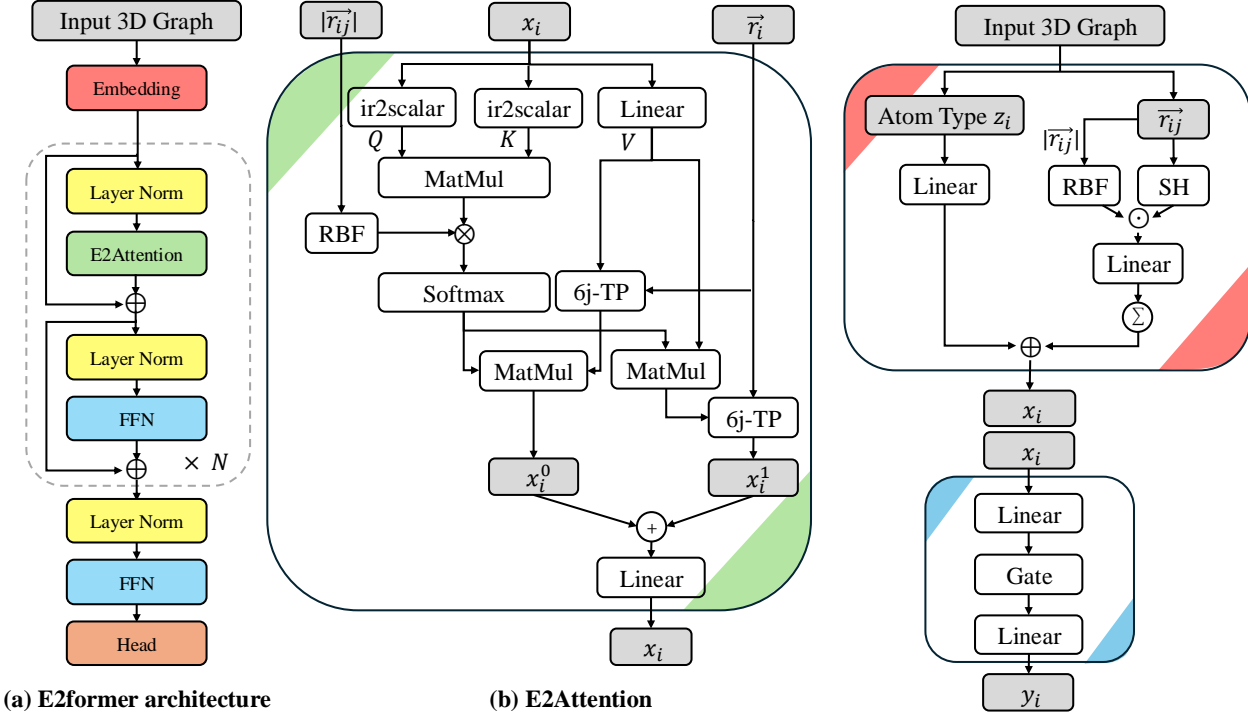


Figure 4. Overview of the E2Former architecture. (a) The main network alternates E2Attention blocks with feedforward layers, repeatedly refining node embeddings from a 3D molecular graph. (b) Within each E2Attention block, scalarized queries/keys (via `ir2scalar`) are combined with distance-dependent features (RBF) and convolutions (6j-TP), updating the node embeddings equivariantly. (c) The final readout incorporates atomic types and radial/spherical expansions (RBF, SH) into a gated projection that produces the per-atom output y_i .

Theorem A.1 (Binomial Local Expansion). Let $\vec{r}_i, \vec{r}_j \in \mathbb{R}^3$ be positions of two nodes i, j in 3D space, and let $\vec{r}_{ij} = \vec{r}_j - \vec{r}_i$. For each integer $\ell \geq 1$, define the real spherical harmonics $Y^{(\ell)}(\vec{r}_{ij})$ of order ℓ evaluated on \vec{r}_{ij} . Then we have:

$$Y^{(\ell)}(\vec{r}_{ij}) = \left[(Y^{(1)}(\vec{r}_j) - Y^{(1)}(\vec{r}_i))^{\otimes \ell} \right]^{(\ell)} = \sum_{u=0}^{\ell} (-1)^{\ell-u} \binom{\ell}{u} \left[Y^{(u)}(\vec{r}_j) \otimes Y^{(\ell-u)}(\vec{r}_i) \right]^{(\ell)},$$

where $[\cdot]^{(\ell)}$ indicates the projection (via Clebsch–Gordan) onto the subspace of total angular momentum ℓ . The symbol “=” reflects an overall normalization factor that depends on the chosen normalization convention for $Y^{(\ell)}$ and for the Clebsch–Gordan products.

Proof. When $\ell = 1$, $Y^{(1)}(\vec{r}_{ij})$ corresponds to p -type spherical harmonics, which are linear in the Cartesian components of (x, y, z) . Since $\vec{r}_{ij} = \vec{r}_j - \vec{r}_i$, we have

$$Y^{(1)}(\vec{r}_j - \vec{r}_i) = Y^{(1)}(\vec{r}_j) - Y^{(1)}(\vec{r}_i),$$

by linearity in coordinates. This fully proves the $\ell = 1$ case.

For $\ell \geq 2$, it is a standard fact that $Y^{(\ell)}$ arises by taking successive Clebsch–Gordan products of $\ell = 1$ irreps. Concretely, one can think of $(x, y, z)^\ell$ monomials projected onto the homogeneous harmonic polynomials of degree ℓ . More precisely, starting with the real p -harmonics (i.e., $Y^{(1)}$), we form

$$(Y^{(1)})^{\otimes \ell} = \underbrace{Y^{(1)} \otimes Y^{(1)} \otimes \dots \otimes Y^{(1)}}_{\ell \text{ times}}.$$

Inside this product, the subspace that transforms irreducibly with total angular momentum ℓ exactly corresponds to $Y^{(\ell)}$. Hence

$$Y^{(\ell)}(\vec{r}_{ij}) \subseteq \left[Y^{(1)}(\vec{r}_{ij}) \right]^{\otimes \ell} \quad (\text{as irreps}),$$

Table 4. Glossary of Notation

Symbol	Description
\mathcal{V}, \mathcal{E}	Set of nodes (vertices) \mathcal{V} and edges \mathcal{E} in a molecular graph.
$ \mathcal{V} , \mathcal{E} $	Number of nodes and edges in the graph, respectively.
N	Often used to denote $ \mathcal{V} $, the number of atoms (nodes).
d	Hidden feature dimension (number of channels) at each spherical degree.
s	Spherical dimension: the number of irreps (from $\ell = 0$ to $\ell = L$).
L, L_{\max}	Maximum angular momentum (highest spherical degree).
$\ell \geq 0, m \in \{-\ell, \dots, \ell\}$	Angular momentum quantum numbers for spherical harmonics.
$Y_m^{(\ell)}(\vec{r})$	Real spherical harmonic of degree ℓ and order m , evaluated at position \vec{r} .
$U^{(\ell)}$	An irreducible representation (irrep) of $SO(3)$ at angular momentum ℓ .
$\mathbf{h}_i \in \mathbb{R}^{s \times d}$	Feature representation of node i , containing scalar/vector components up to spherical degree L .
$\vec{r}_{ij} \in \mathbb{R}^3$	Relative position vector from node i to node j .
\otimes	Clebsch–Gordan (CG) tensor product of two irreps.
\otimes^{6j}	Wigner $6j$ -based tensor product (recoupling) of irreps, reorganizing the CG couplings.
α_{ij}	Attention coefficient between node i and j in an equivariant attention layer.
$C_{\ell_1 m_1, \ell_2 m_2}^{(\ell_3 m_3)}$	Clebsch–Gordan coefficient coupling two irreps ℓ_1, ℓ_2 to an output irreps ℓ_3 .
$\begin{pmatrix} \ell_1 & \ell_2 & \ell_3 \\ m_1 & m_2 & m_3 \end{pmatrix}$	Wigner $3j$ symbol (equivalently related to Clebsch–Gordan coefficients).
$\begin{Bmatrix} j_1 & j_2 & j_3 \\ j_4 & j_5 & j_6 \end{Bmatrix}$	Wigner $6j$ symbol, governing recoupling of three angular momenta in different orders.
$D^{(\ell)}(R)$	Wigner D -matrix describing how spherical harmonics of degree ℓ transform under rotation R .
$SO(3)$	3D rotation group; E2Former is equivariant to transformations in $SO(3)$.
E2Former	The proposed Efficient and Equivariant Transformer architecture.
Wigner $6j$ Conv	The core convolution module leveraging Wigner $6j$ recoupling to shift edge-based operations to nodes.

up to an overall multiplicative constant from normalization.

For $\ell = 1$, we know

$$Y^{(1)}(\vec{r}_{ij}) = Y^{(1)}(\vec{r}_j) - Y^{(1)}(\vec{r}_i).$$

Therefore,

$$(Y^{(1)}(\vec{r}_{ij}))^{\otimes \ell} = (Y^{(1)}(\vec{r}_j) - Y^{(1)}(\vec{r}_i))^{\otimes \ell}.$$

Expanding the right-hand side entrywise using the binomial theorem,

$$(Y^{(1)}(\vec{r}_j) - Y^{(1)}(\vec{r}_i))^{\otimes \ell} = \sum_{u=0}^{\ell} (-1)^{\ell-u} \binom{\ell}{u} [(Y^{(1)}(\vec{r}_j))^{\otimes u} \otimes (Y^{(1)}(\vec{r}_i))^{\otimes (\ell-u)}].$$

We now identify $[\cdot]^{(\ell)}$ as the usual projection onto the total angular momentum ℓ subspace from the Clebsch–Gordan decomposition. Namely,

$$(Y^{(1)}(\vec{r}_j))^{\otimes u} \rightarrow \sum_{k \text{ allowed}} Y^{(k)}(\vec{r}_j),$$

where k ranges from 0 to u but we only keep the term $k = u$ if we want the highest possible rank from u copies of $\ell = 1$. Denote $Y^{(u)}(\vec{r}_j)$ the rank- u irreps embedded in $(Y^{(1)}(\vec{r}_j))^{\otimes u}$. Likewise for $Y^{(1)}(\vec{r}_i)^{\otimes (\ell-u)}$. Then restricting to the total ℓ subspace,

$$[(Y^{(1)}(\vec{r}_j))^{\otimes u} \otimes (Y^{(1)}(\vec{r}_i))^{\otimes (\ell-u)}]^{(\ell)} = [Y^{(u)}(\vec{r}_j) \otimes Y^{(\ell-u)}(\vec{r}_i)]^{(\ell)},$$

where the bracket $[\cdot]^{(\ell)}$ extracts the ℓ -th order irrep out of the possible sums. Putting it all together, we indeed obtain

$$[(Y^{(1)}(\vec{r}_j) - Y^{(1)}(\vec{r}_i))^{\otimes \ell}]^{(\ell)} = \sum_{u=0}^{\ell} (-1)^{\ell-u} \binom{\ell}{u} [Y^{(u)}(\vec{r}_j) \otimes Y^{(\ell-u)}(\vec{r}_i)]^{(\ell)}.$$

Since $Y^{(\ell)}(\vec{r}_{ij})$ is (up to a constant) the rank- ℓ subspace of $(Y^{(1)}(\vec{r}_{ij}))^{\otimes \ell}$, and we have replaced $Y^{(1)}(\vec{r}_{ij})$ by $Y^{(1)}(\vec{r}_j) - Y^{(1)}(\vec{r}_i)$, the two sides are equal up to that normalization factor. This completes the argument. \square

Table 5. Hyperparameter Configuration for E2Former on OC20, OC22, and SPICE

Hyperparameter	E2Former 33M	E2Former 67M	Description
— General Training Settings —			
optim.lr.initial	0.00015	0.0002	Initial learning rate for the optimizer.
optim.batch_size	128 for OC20/OC22 and 48 for SPICE	64	Training batch size.
— Model Architecture —			
model.backbone.encoder_embed_dim	256	256	Embedding dimension for each node.
model.backbone.hidden_size	256	256	Hidden size for intermediate layers.
model.backbone.num_layers	6	12	Number of E2Former layers.
model.backbone.max_neighbors	20	20	Max neighbors per node for message passing.
model.backbone.irreps_node_embedding	256x0e+256x1e+256x2e+256x3e	256x0e+256x1e+256x2e+256x3e	Irreps for node embeddings up to $\ell = 3$.
model.backbone.irreps_head	16x0e+16x1e+16x2e+16x3e	16x0e+16x1e+16x2e+16x3e	Irreps for the final head up to $\ell = 3$.
model.backbone.attn.scalar_head	16	16	Size of scalar attention head projections.
model.backbone.num_attn_heads	32	32	Number of multi-head attentions per layer.
model.backbone.number_of_basis	256	256	Number of radial basis functions.
model.backbone.max_radius	12 for OC20/22 and 5 for SPICE	12 for OC20/22 and 5 for SPICE	Cutoff radius for local neighborhood.
model.backbone.alpha_drop	0.05	0.05	Drop rate for alpha (e.g., attention dropout).
model.backbone.drop_path_rate	0.05	0.05	Stochastic depth/drop path rate.
model.backbone.basis_type	gaussiansmear	gaussiansmear	Type of radial embedding (Gaussian smearing).
model.backbone.norm_layer	layer_norm_sh	layer_norm_sh	Normalization layer type (LayerNorm in spherical basis).
model.backbone.attn_type	all-order	all-order	Attention mechanism covering all spherical orders.
model.backbone.tp_type	dot_alpha	dot_alpha	Type of tensor product (dot + learned scale).
model.backbone.ffn_type	s2	s2	Type of feed-forward network in each block.

A.1. Wigner $6j$ Recoupling and Node-Based Factorization

Setup: We consider a typical $SO(3)$ -equivariant Transformer layer that performs message passing from each node j in the neighborhood of i using the tensor product $\mathbf{h}_j \otimes Y^{(\ell)}(\vec{r}_{ij})$. An *attention weight* α_{ij} modulates the contribution of node j to node i . Symbolically,

$$\mathbf{h}_i^{\text{new}} = \sum_{j \in \mathcal{N}(i)} \alpha_{ij} (\mathbf{h}_j \otimes Y^{(\ell)}(\vec{r}_{ij})).$$

Goal: To show that the expensive edge-based computation over (i, j) can be reorganized so that the *tensor product* portion (or at least the dominating part of it) depends only on node i and a separate node j portion. This is achieved by:

$$Y^{(\ell)}(\vec{r}_{ij}) \mapsto \sum_{u=0}^{\ell} [Y^{(u)}(\vec{r}_i)] \otimes^{6j} [Y^{(\ell-u)}(\vec{r}_j)],$$

together with a rearrangement (via Wigner $6j$) of \mathbf{h}_j inside the product.

Theorem A.2 (Node-Based Factorization via Wigner $6j$). *Let $\mathbf{h}_j \in \mathbb{R}^d$ be the feature of node j , and let α_{ij} be any scalar weight (e.g. an attention coefficient). In the $SO(3)$ -equivariant layer:*

$$\sum_{j \in \mathcal{N}(i)} \alpha_{ij} (\mathbf{h}_j \otimes Y^{(\ell)}(\vec{r}_{ij})),$$

we can reorganize $Y^{(\ell)}(\vec{r}_{ij})$ into node- i and node- j parts by Theorem A.1 and then apply Wigner $6j$ recoupling to obtain:

$$\sum_{j \in \mathcal{N}(i)} \alpha_{ij} (\mathbf{h}_j \otimes Y^{(\ell)}(\vec{r}_{ij})) = \sum_{u=0}^{\ell} [Y^{(u)}(\vec{r}_i)] \otimes^{6j} \left(\sum_{j \in \mathcal{N}(i)} \alpha_{ij} [\mathbf{h}_j \otimes Y^{(\ell-u)}(\vec{r}_j)] \right),$$

up to a constant factor that depends on binomial coefficients and the chosen normalization of the spherical harmonics.

Proof. From Theorem A.1, we have

$$Y^{(\ell)}(\vec{r}_{ij}) = \sum_{u=0}^{\ell} (-1)^{\ell-u} \binom{\ell}{u} [Y^{(u)}(\vec{r}_i) \otimes Y^{(\ell-u)}(\vec{r}_j)]^{(\ell)},$$

where $[\cdot]^{(\ell)}$ is projection on the ℓ -th order subspace. Substituting inside the sum yields

$$\sum_{j \in \mathcal{N}(i)} \alpha_{ij} (\mathbf{h}_j \otimes Y^{(\ell)}(\vec{r}_{ij})) = \sum_{j \in \mathcal{N}(i)} \alpha_{ij} \mathbf{h}_j \otimes \sum_{u=0}^{\ell} (-1)^{\ell-u} \binom{\ell}{u} [Y^{(u)}(\vec{r}_i) \otimes Y^{(\ell-u)}(\vec{r}_j)]^{(\ell)}.$$

Rewriting,

$$= \sum_{u=0}^{\ell} (-1)^{\ell-u} \binom{\ell}{u} \sum_{j \in \mathcal{N}(i)} \left(\alpha_{ij} \mathbf{h}_j \otimes [Y^{(u)}(\vec{r}_i) \otimes Y^{(\ell-u)}(\vec{r}_j)]^{(\ell)} \right).$$

We note that \mathbf{h}_j is a (possibly) lower-rank $\ell = 0$ representation in the sense it transforms as a scalar or some fixed representation. To rearrange, we use the fact that CG products are associative up to Wigner $6j$ constants. Symbolically, for any triple of irreps $U^{(a)}, U^{(b)}, U^{(c)}$,

$$(U^{(a)} \otimes U^{(b)}) \otimes U^{(c)} \longleftrightarrow U^{(a)} \otimes (U^{(b)} \otimes U^{(c)}),$$

with the passage from one to the other governed by $6j$ symbols (plus some phase factors). Concretely, we reorder \mathbf{h}_j with $Y^{(u)}(\vec{r}_i)$ so that $Y^{(u)}(\vec{r}_i)$ is ‘‘factored out’’ on the left, while \mathbf{h}_j becomes coupled to $Y^{(\ell-u)}(\vec{r}_j)$ on the right:

$$(\mathbf{h}_j \otimes Y^{(u)}(\vec{r}_i)) \otimes Y^{(\ell-u)}(\vec{r}_j) \xrightarrow{(\text{commute}+6j)} Y^{(u)}(\vec{r}_i) \otimes^{6j} (\mathbf{h}_j \otimes Y^{(\ell-u)}(\vec{r}_j)).$$

Hence each term in the sum can be expressed as

$$Y^{(u)}(\vec{r}_i) \otimes^{6j} (\mathbf{h}_j \otimes Y^{(\ell-u)}(\vec{r}_j)),$$

where the overall $6j$ symbol also takes into account the $(-1)^{\ell-u}$ and $\binom{\ell}{u}$ factors. Summing over all $j \in \mathcal{N}(i)$ and all u yields

$$\sum_{u=0}^{\ell} Y^{(u)}(\vec{r}_i) \otimes^{6j} \left(\sum_{j \in \mathcal{N}(i)} \alpha_{ij} \mathbf{h}_j \otimes Y^{(\ell-u)}(\vec{r}_j) \right).$$

As stated, the binomial factors can be merged into the $6j$ coefficients, so from a purely formal standpoint we get

$$\sum_{j \in \mathcal{N}(i)} \alpha_{ij} (\mathbf{h}_j \otimes Y^{(\ell)}(\vec{r}_{ij})) = \sum_{u=0}^{\ell} [Y^{(u)}(\vec{r}_i)] \otimes^{6j} \left(\sum_{j \in \mathcal{N}(i)} \alpha_{ij} [\mathbf{h}_j \otimes Y^{(\ell-u)}(\vec{r}_j)] \right),$$

up to a constant that we can fix based on normalization. This completes the factorization. \square

Remark A.3. The upshot is that (i) the node-local spherical harmonics $Y^{(u)}(\vec{r}_i)$ can be precomputed once for each node i , and (ii) the partial sum $\sum_j \alpha_{ij} (\mathbf{h}_j \otimes Y^{(\ell-u)}(\vec{r}_j))$ can be treated as a single node-based operation. Thus, the scale of the computation is controlled by $|\mathcal{V}|$ (the number of nodes) rather than $|\mathcal{E}|$ (the number of edges), assuming we can handle \otimes^{6j} at the node level efficiently. This is precisely the core reason E2Former achieves improved scalability compared to conventional $\text{SO}(3)$ -equivariant Transformers that do edge-level spherical harmonic products.

A.2. Wigner $3j$ and $6j$ Symbols

The Wigner $3j$ and $6j$ symbols encapsulate the recoupling properties of angular momenta in quantum mechanics and the representation theory of the Lie group $\text{SU}(2)$. These symbols serve as transformation coefficients in the decomposition of tensor products of irreducible representations, encoding symmetry properties that facilitate calculations in angular momentum coupling.

A.3. Definition and Properties of the Wigner $3j$ Symbol

The Wigner $3j$ symbol is denoted as

$$\begin{pmatrix} j_1 & j_2 & j_3 \\ m_1 & m_2 & m_3 \end{pmatrix}, \quad (6)$$

The selection rules impose the constraints $m_1 + m_2 + m_3 = 0$, as well as the triangular inequalities $|j_1 - j_2| \leq j_3 \leq j_1 + j_2$.

Explicitly, the $3j$ symbol admits the summation representation

$$\begin{pmatrix} j_1 & j_2 & j_3 \\ m_1 & m_2 & m_3 \end{pmatrix} = \delta(m_1 + m_2 + m_3, 0) (-1)^{j_1 - j_2 - m_3} \quad (7)$$

$$\times \sqrt{\frac{(j_1 + j_2 - j_3)!(j_1 - j_2 + j_3)!(-j_1 + j_2 + j_3)!}{(j_1 + j_2 + j_3 + 1)!}} \quad (8)$$

multiplied by an additional factorial term involving $(j_1 \pm m_1)!$, $(j_2 \pm m_2)!$, and $(j_3 \pm m_3)!$, along with a finite summation over an integer index ensuring non-negative factorial arguments.

The $3j$ symbol satisfies notable symmetry properties: invariance under even permutations of columns, sign changes under certain odd permutations, and a time-reversal symmetry given by

$$\begin{pmatrix} j_1 & j_2 & j_3 \\ -m_1 & -m_2 & -m_3 \end{pmatrix} = (-1)^{j_1+j_2+j_3} \begin{pmatrix} j_1 & j_2 & j_3 \\ m_1 & m_2 & m_3 \end{pmatrix}. \quad (9)$$

Moreover, these symbols satisfy orthogonality relations of the form

$$\sum_{m_1, m_2} (2j_3 + 1) \begin{pmatrix} j_1 & j_2 & j_3 \\ m_1 & m_2 & m_3 \end{pmatrix} \begin{pmatrix} j_1 & j_2 & j_3 \\ m_1 & m_2 & m'_3 \end{pmatrix} = \delta_{m_3, m'_3}. \quad (10)$$

A.4. Definition and Properties of the Wigner $6j$ Symbol

The Wigner $6j$ symbol extends the recoupling properties to three angular momenta, appearing in transformations between different coupling sequences. It is defined via the summation over four $3j$ symbols:

$$\begin{Bmatrix} j_1 & j_2 & j_3 \\ j_4 & j_5 & j_6 \end{Bmatrix} = \sum_{m_1, \dots, m_6} (-1)^{\sum_{k=1}^6 (j_k - m_k)} \begin{pmatrix} j_1 & j_2 & j_3 \\ -m_1 & -m_2 & -m_3 \end{pmatrix} \begin{pmatrix} j_1 & j_5 & j_6 \\ m_1 & -m_5 & m_6 \end{pmatrix} \quad (11)$$

$$\times \begin{pmatrix} j_4 & j_2 & j_6 \\ m_4 & m_2 & -m_6 \end{pmatrix} \begin{pmatrix} j_4 & j_5 & j_3 \\ -m_4 & m_5 & m_3 \end{pmatrix}. \quad (12)$$

Alternatively, it relates to the Racah W -coefficient as

$$\begin{Bmatrix} j_1 & j_2 & j_3 \\ j_4 & j_5 & j_6 \end{Bmatrix} = (-1)^{j_1+j_2+j_4+j_5} W(j_1 j_2 j_5 j_4; j_3 j_6). \quad (13)$$

The Racah coefficient, denoted as $W(j_1 j_2 j_5 j_4; j_3 j_6)$, represents a transformation coefficient associated with recoupling two different schemes of combining three angular momenta. It is directly related to the $6j$ symbol by a simple phase factor, as given above.

The $6j$ symbol is invariant under all permutations of its columns and the simultaneous exchange of upper and lower indices in any two columns. These properties reflect the tetrahedral symmetry of the corresponding Yutsis graph.

Orthogonality relations include:

$$\sum_{j_3} (2j_3 + 1) \begin{Bmatrix} j_1 & j_2 & j_3 \\ j_4 & j_5 & j_6 \end{Bmatrix} \begin{Bmatrix} j_1 & j_2 & j_3 \\ j_4 & j_5 & j'_6 \end{Bmatrix} = \frac{\delta_{j_6, j'_6}}{2j_6 + 1} \{j_1 \ j_5 \ j_6\} \{j_4 \ j_2 \ j_6\}. \quad (14)$$

The Ponzano–Regge asymptotic formula expresses the $6j$ symbol in terms of the geometry of a tetrahedron whose edge lengths correspond to $j_1 + \frac{1}{2}, \dots, j_6 + \frac{1}{2}$, illustrating the connection between quantum angular momentum and semiclassical geometry.

The Racah coefficients also satisfy orthogonality and symmetry properties analogous to those of the $6j$ symbols and play a fundamental role in simplifying calculations involving multiple angular momenta.